3D element imaging using NSECT for the detection of renal cancer: a simulation study in MCNP

# 3D element imaging using NSECT for the detection of renal cancer: a simulation study in MCNP

**R S Viana**[1,2]**, G A Agasthya**[1,3]**, H Yoriyaz**[2] **and A J Kapadia**[1,4]

[1] Carl E Ravin Advanced Imaging Laboratories, Department of Radiology, Duke University, Durham, NC, USA
[2] Nuclear Engineering Center, Nuclear Energy Research Institute, IPEN-CEN/SP, São Paulo, Brazil
[3] Department of Biomedical Engineering, Duke University, Durham, NC, USA
[4] Medical Physics Graduate Program, Duke University, Durham, NC, USA

E-mail: rodrigossviana@gmail.com and anuj.kapadia@duke.edu

## Abstract

This work describes a simulation study investigating the application of neutron stimulated emission computed tomography (NSECT) for noninvasive 3D imaging of renal cancer *in vivo*. Using MCNP5 simulations, we describe a method of diagnosing renal cancer in the body by mapping the 3D distribution of elements present in tumors using the NSECT technique. A human phantom containing the kidneys and other major organs was modeled in MCNP5. The element composition of each organ was based on values reported in literature. The two kidneys were modeled to contain elements reported in renal cell carcinoma (RCC) and healthy kidney tissue. Simulated NSECT scans were executed to determine the 3D element distribution of the phantom body. Elements specific to RCC and healthy kidney tissue were then analyzed to identify the locations of the diseased and healthy kidneys and generate tomographic images of the tumor. The extent of the RCC lesion inside the kidney was determined using 3D volume rendering. A similar procedure was used to generate images of each individual organ in the body. Six isotopes were studied in this work—$^{32}$S, $^{12}$C, $^{23}$Na, $^{14}$N, $^{31}$P and $^{39}$K. The results demonstrated that through a single NSECT scan performed *in vivo*, it is possible to identify the location of the kidneys and other organs within the body, determine the extent of the tumor within the organ, and to quantify the differences between cancer and healthy tissue-related isotopes with $p \leqslant 0.05$. All of the images demonstrated appropriate concentration changes between the organs, with some discrepancy observed in $^{31}$P, $^{39}$K and $^{23}$Na. The discrepancies were likely due to the low concentration of the elements in the tissue that were below the current detection sensitivity of the NSECT technique.

(Some figures may appear in colour only in the online journal)

## 1. Introduction

Renal cancer is one of the ten most common cancers in humans. According to the American Cancer Society, approximately 65 150 patients will be diagnosed with renal cancer in the United States in 2013, of which 13 680 will die due to direct or indirect causes related to the disease (ACN 2013). The difficulty in obtaining an accurate diagnosis of kidney cancer lies in the fact that it presents symptoms that are not unique to the disease and can be misdiagnosed as other diseases; for example, flank pain, hematuria, palpable abdominal mass, fatigue, weight loss, and anemia. Due to these characteristics, the detection of renal cancer is incidental, often detected via abdominal radiographic examinations conducted for other health conditions.

While several noninvasive imaging techniques have been proposed to detect cancers and differentiate between benign and malignant tumors (Zhang *et al* 2007, Kim *et al* 2004, 2008, 2009, 2010, Verma *et al* 2010), according to Millet *et al* (2011), no substantial criteria have been developed to distinguish noninvasively between a malignant and benign tumor *in vivo*. Furthermore, conventional medical images alone are insufficient to differentiate between benign and malignant tumors. Presently, biopsy remains the most reliable technique for detection despite being an invasive and unpleasant procedure that carries considerable risk for the patient (Neuzillet *et al* 2004, Schmidbauer *et al* 2008, Remzi and Marberger 2009, Pandharipande *et al* 2010). There is a need for a noninvasive technique to detect renal cell carcinoma (RCC) *in vivo*. While biopsy is reliable for confirming a diagnosis, imaging methods are generally considered satisfactory for the detection of kidney cancer. In this study, we propose the application of a novel noninvasive imaging technique to detect renal cancer *in vivo* and differentiate between normal and malignant kidney tissue.

In previous work, we described a new technique called neutron stimulated emission computed tomography (NSECT), a noninvasive tomographic imaging method of measuring elements in the body (Floyd *et al* 2006). NSECT is based on the principle of fast-neutron inelastic scattering, which can be explained as follows: When a fast neutron strikes a naturally-occurring atomic nucleus in the body, it excites the nucleus to a higher energy level. The excitation is followed by nuclear decay along with characteristic gamma emission from the nucleus. The energy of the characteristic gamma can be used to generate a quantitative spectrum of the elemental composition of the sample. NSECT can thus be used to detect and quantify elements that occur in the human body without the need for any radioactive tracers or other injections.

NSECT images are generated by performing a tomographic scan of the sample using a narrow collimated neutron beam (Floyd *et al* 2008). Sinograms are generated for each element of interest and are then reconstructed using a suitable image reconstruction technique. The elements that can be identified using the NSECT technique depend on the incident neutron energy used, which is typically between 5–10 MeV. This energy is sufficient to detect almost all elements that occur in the human body. Such element identification can be used to detect several diseases that are characterized by differences in elements between healthy and normal tissue. For example, differences in Ca, V, Cu, Zn, Se and Rb have been reported in breast cancer between benign and malignant tissues (Rizk and Sky-Peck 1984); Fe and Cu in liver iron and copper overload (Kapadia 2007), and Fe, Al, Zn Cu and Hg in plaques in Alzheimer's disease (Mutter 2008), Li, Cd, Pb, Ti and Rb in kidney diseases (Dobrowolski *et al* 2002, Chmielnicka and Nasiadek 2003, Calvo *et al* 2009) and Cu, Fe, Zn and Se in heart diseases (Altekin *et al* 2005).

The utility of the NSECT technique has previously been successfully demonstrated for the detection of breast cancer (Kapadia *et al* 2008a), breast microcalcifications (Viana and Yoriyaz 2011) and iron overload in liver (Kapadia *et al* 2008b, Agasthya *et al* 2012). Here, we
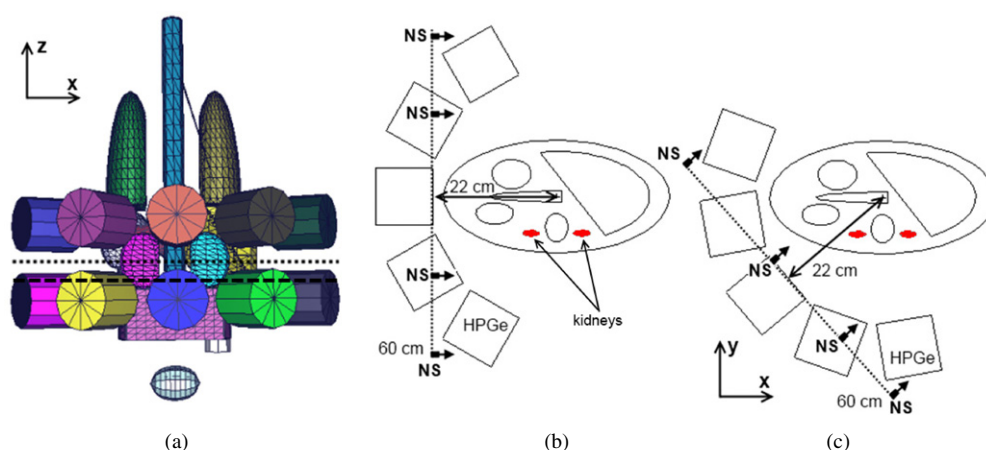
(a)     (b)     (c)

**Figure 1.** The 3D view showing the back of the anatomical phantom and the acquisition system (a). The dotted line shows the neutron source translation path. The torso in this figure was made invisible to improve the 3D view of the internal organs. The 2D top view of the acquisition system at a rotation of 40° (b) and 0° (c). Both images correspond to the plane represented by the dashed line in (a). The location of kidneys is shown in red. NS represents the neutron source firing the beam into the phantom perpendicular to the translation path (dotted line in (a)).

demonstrate its potential utility in 3D imaging of RCC *in vivo* using Monte Carlo simulations in MCNP5.

## 2. Methodology

In this section we describe the Monte Carlo simulations used to model the anatomical phantom of RCC and the NSECT acquisition system, the procedure used to generate the sinograms for tomographic reconstructions, and the methods used for spectral analysis. The simulations described in this work were performed using MCNP5 (X-5 2003).

The MCNP code is a well-known and widely used Monte Carlo code for neutron, photon, and electron transport simulations. The first MCNP version was released in the mid-1970s for neutron and photon transport, and it was enhanced over the years to include electron physics and coupled electron–photon calculations, macro-body geometry, and statistical convergence tests. The present work uses the fifth release of the MCNP code—MCNP5.

The MCNP5 code requires an input file, which allows the user to specify the geometry, source specifications, material compositions, nuclear data library and the parameters to be estimated. The geometry models a set of mathematical surfaces to create different volumes to represent the organs of the human body and the NSECT acquisition system (which includes the neutron source and detection system). The details of the MCNP5 model and overall methodology are discussed below in the following order: anatomical phantom, acquisition system, tomographic reconstruction, and data analysis.

### 2.1. Anatomical phantom

The anatomical phantom adopted in this work is a human mathematical phantom originally developed by Cristy and Eckerman (1987) (shown in figure 1). The organs in the phantom are represented by a set of mathematical functions and correspond to organs in an average adult male. The following organs were modeled in the torso to simulate realistic human anatomy:

**Table 1.** Material composition from Calvo *et al* (2009) for RCC and healthy kidney used in the Monte Carlo modeling. Both kidneys were modeled assuming the shape, size and density of an adult kidney (density 1.05 g cm$^{-3}$).

| Element | RCC lesion[a] (% mass fraction $\pm \sigma$) | Healthy kidney[a] (% mass fraction $\pm \sigma$) | RCC lesion versus healthy kidney[d] |
|---|---|---|---|
| Al | 8.10E-04 $\pm$ 7.00E-06 | <4.60E-06[b] | <0.01 |
| Ca | 5.10E-02 $\pm$ 9.30E-05 | 3.30E-02 $\pm$ 3.03E-04 | <0.01 |
| Cd | 2.30E-04 $\pm$ 1.70E-06 | 1.40E-03 $\pm$ 8.00E-06 | <0.01 |
| Cr | 1.30E-04 $\pm$ 2.00E-06 | <5.00E-07 | <0.05 |
| Cu | 8.00E-04 $\pm$ 1.70E-06 | 8.30E-04 $\pm$ 9.00E-06 | NS |
| Fe | 2.50E-02 $\pm$ 5.90E-05 | 3.20E-02 $\pm$ 2.19E-04 | <0.01 |
| K | 5.00E-03 $\pm$ 5.00E-06 | 1.60E-02 $\pm$ 3.57E-04 | <0.05 |
| Mg | 6.60E-03 $\pm$ 1.40E-05 | 9.90E-03 $\pm$ 1.96E-04 | <0.01 |
| Mn | 9.80E-05 $\pm$ 6.00E-07 | 9.20E-05 $\pm$ 4.00E-07 | NS |
| Na | 1.00E-02 $\pm$ 1.31E-04 | 1.60E+00 $\pm$ 7.28E-03 | <0.001 |
| P | 6.30E-02 $\pm$ 1.87E-04 | 4.30E-03 $\pm$ 3.10E-05 | <0.001 |
| Pb | 1.70E-04 $\pm$ 2.00E-06 | <5.00E-06 | <0.05 |
| Zn | 2.50E-02 $\pm$ 3.79E-04 | <7.00E-06 | <0.001 |
| H[c] | 1.03E+01 | 1.02E+01 | – |
| C[c] | 1.33E+01 | 1.30E+01 | – |
| Cl[c] | 2.00E-01 | 2.00E-01 | – |
| S[c] | 2.00E-01 | 2.00E-01 | – |
| N[c] | 3.00E+00 | 3.00E+00 | – |
| O[c] | 7.28E+01 | 7.16E+01 | – |

[a] The values reported in Calvo *et al* (2009) are in ppm and have been converted to % mass fraction for this work.
[b] Values shown with '<' represent an upper limit of concentration for the material.
[c] Composition from ICRU (1992). The comparison of concentration between tissues is not available.
[d] *P*-value. NS means the statistical difference is not significant.

**Table 2.** Material composition of other organs around the kidneys. The symbol '*' denotes the composition from ICRP (2009), whereas the remaining compositions are from ICRU (1992).

| Organ | Elemental composition (%) | | | | | | | | | | | | Density (g cm$^{-3}$) |
|---|---|---|---|---|---|---|---|---|---|---|---|---|---|
| | H | C | N | O | Na | P | S | Cl | K | Mg | Ca | Fe | |
| Soft tissue | 10.5 | 25.6 | 2.7 | 60.2 | 0.1 | 0.2 | 0.3 | 0.2 | 0.2 | – | – | – | 1.03 |
| Spine | 3.4 | 15.5 | 4.2 | 43.5 | 0.1 | 10.3 | 0.3 | – | – | 0.2 | 22.5 | – | 1.92 |
| Liver | 10.2 | 13.9 | 3.0 | 71.6 | 0.2 | 0.3 | 0.3 | 0.2 | 0.3 | – | – | – | 1.06 |
| Stomach* | 10.5 | 11.4 | 2.5 | 74.9 | 0.1 | 0.1 | 0.1 | 0.2 | 0.1 | – | – | – | 1.04 |
| Gallbladder* | 10.3 | 17.0 | 3.1 | 68.7 | 0.1 | 0.1 | 0.2 | 0.3 | 0.2 | – | – | 0.1 | 1.03 |
| Spleen* | 10.2 | 11.1 | 3.3 | 74.3 | 0.1 | 0.2 | 0.2 | 0.3 | 0.2 | – | – | 0.1 | 1.04 |

kidneys, spine, gallbladder, liver, stomach and spleen. The material composition of each organ was based on ICRU (1992) and ICRP (2009) reports, which provide the compositions of normal human organs including the kidneys (shown in table 2). The composition of the RCC tissue was modeled by changing the elemental concentrations of the ICRU (1992) renal tissue to reflect the elemental changes through the mean profile of elements in RCC tissue compared against healthy kidney cortex, shown in table 1. These compositions were taken from 70 patients diagnosed with kidney tumors in different stages ranging from stage 1 to stage 4 according to the TNM classification. The mean profile of the lesion composition was obtained by averaging all patients (Calvo *et al* 2009). The torso composition was modeled using soft tissue from ICRU 46.

Of the two kidneys in the phantom, one was modeled as healthy and the other contained RCC tissue. RCC tumors in advanced stages are known to exhibit considerably large dimensions; for example, a stage II tumor typically exceeds 7 cm in its greatest dimension (Cohen and McGovern 2005). Thus, the modeling of the whole kidney as cancerous can be considered representative of late stages of the disease. In this study, the right kidney was modeled as healthy and the left kidney as cancerous.

### 2.2. Acquisition system

*Detectors.* The detection system modeled in this work contained ten high-purity germanium (HPGe) detectors arranged around the phantom in two semi-circular rings of 22 cm radius (figures 1(a)–(c)). Each semi-circular arrangement contained five detectors angled at $30°$ from each other and with respect to the *x*-axis. The 22 cm radius was chosen to allow sufficient room for translation and rotation of the torso phantom for tomographic acquisition. A 4 cm gap (represented by the dotted line in figure 1(a)) was left between the two semi-circular rows of detectors to allow the neutron beam to pass without direct incidence on the detectors. Each detector was modeled as a cylinder of 10 cm diameter and 10 cm height and contained 100% germanium with natural density. This composition is similar to the composition of commercially available HPGe detectors in terms of the germanium concentration. However, *p*-type or *n*-type doping was not considered in this study. Detector efficiency was modeled at 100%, i.e., every photon that interacted in the germanium crystal was tracked and reported the energy deposited through the interactions. Therefore, germanium crystal efficiency was modeled realistically, but all other detector-related efficiency losses were ignored. However, dose calculations were performed and reported taking into account the lower efficiency of realistic HPGe detectors ($\sim$25% efficiency).

The detectors setup was chosen with three goals in mind: (a) to maximize the efficiency of photon detection, (b) to minimize the Compton scattering between detectors, and (c) to minimize the probability of direct neutron incidence onto the detectors.

*Source.* The neutron source was modeled as a collimated, mono-energetic neutron emitter emitting 5 MeV neutrons. The energy (5 MeV) was chosen to stimulate most isotopes of interest to RCC including $^{12}C$ at 4.439 MeV. The beam cross section was set to 1 $cm^2$ to achieve sufficient resolution in the reconstructed image as well as allow reasonable flux when using a real neutron source in physical experiments.

The acquisition system and the anatomical phantom were surrounded by air. Figure 1 shows 3D (a) and 2D (b and c) views of the acquisition system and the anatomical phantom.

### 2.3. Tomographic acquisition and reconstruction

In this section we describe the tomographic acquisition and image reconstruction protocol used in the simulation. Tomographic scanning was performed in a similar manner as first generation CT (translate–rotate configuration). The neutron beam and detectors were rotated around the anatomical phantom in ten discrete angular steps from $0°$ to $180°$ in $20°$ increments. At each angular position, the neutron beam was translated linearly through 60 cm in fixed steps of 1 cm (to cover the span of the torso). After the final translation step, the acquisition system (i.e., all detectors and the neutron source) was rotated by $20°$ to the next angular position, and the translation step was repeated again. The acquisition process is shown for two discrete angular positions ($40°$ and $0°$) in figures 1(b) and (c). The total scan comprised 60 translations at 10 angular positions, for a total of 600 beam positions per slice. Ten slices of 1 cm thickness

were acquired over the torso to cover the height of the kidneys. The total dose from this ten-slice scan was determined to be less than 4 mSv. In a real scan, the neutron fluence from a commercial neutron generator ranges from $10^7$ to $10^{10}$ n s$^{-1}$. Assuming a fluence requirement of $10^7$ neutrons per beam projection, the scan time for 6000 beam projections could range between 1–10 min depending on the type of neutron generator used and the efficiency of collimation.

In contrast with conventional CT that is acquired over 360°, an NSECT acquisition can be satisfactorily performed over 180° because the tissue within the neutron beam path undergoes stimulated emission regardless of the beam orientation. Therefore, scanning over 360° would simply duplicate the data acquired, which would provide the advantage of lower noise but at the cost of higher dose and longer scan time. We have shown previously that a 180° acquisition is sufficient to generate clinically useful images (Floyd *et al* 2008). In the current case, the beam orientation was strategically set in order to illuminate the closest half of the body where the kidneys are located. This orientation ensured a high signal-to-noise ratio by reducing the amount of photon scatter in the backward detectors. In this orientation, the photons emitted by the kidneys will travel through the body and reach the detection system through the shortest path.

As a consequence of Monte Carlo method, the results obtained using MCNP5 are automatically normalized by the source intensity. Therefore, without knowing *a priori* the number of neutrons emitted by the source, all results from MCNP5 simulations must be interpreted as a ratio between the desired quantity (dose, flux or pulse height) and the source intensity. To achieve a real number, all results were normalized to $10^7$ neutrons per beam projection, which is typical of a real NSECT scan and sufficient to image most isotopes in the body (Kapadia *et al* 2008b)

At each projection, we acquired a complex photon spectrum composed of multiple peaks corresponding to different isotopes in the sample and the acquisition system. In order to suppress noise, a background correction technique was applied to each spectrum (Floyd *et al* 2007). After background correction, the resulting spectra were analyzed to identify the peaks corresponding to the isotopes of interest. Based on prior information about the composition of the irradiated tissue and the known energy levels from excited states of the isotopes of interest (NUDAT 2013), the peaks in the corrected spectra for all projections were matched with the corresponding energy states of interest. The height of each selected peak was then extracted and used to generate a sinogram corresponding to the concentration of the isotopes of interest in the irradiated tissue. Such sinograms were generated for the following six different isotopes that have been associated with RCC: $^{32}$S, $^{12}$C, $^{23}$Na, $^{14}$N, $^{31}$P and $^{39}$K.

Considering the tissue composition for both kidneys shown in table 1, the isotopes of interest were selected from three regions of interest (ROIs) in the image: (a) background (i.e., bulk isotopes $^{32}$S, $^{12}$C, and $^{14}$N present in the human body), (b) RCC kidney (i.e., isotope present in higher concentration in RCC—$^{31}$P), and (c) healthy kidney (i.e., isotopes present in higher concentration in healthy kidney—$^{23}$Na and $^{39}$K). The background ROI (a) was required to establish a baseline for the isotopes that were common in all three regions. The isotopes selected for (b) and (c) were analyzed in these regions to identify the kidneys as well as the RCC lesion within the torso. All of the isotopes and their respective energies evaluated in this work are described in table 3.

The image reconstruction was carried out using the expectation-maximization (EM) algorithm (Lange and Carson 1984) with 15 iterations for a 128 × 128 pixel image. The EM algorithm is well known for its application in reconstructing Poisson distributed signals and has been used successfully for NSECT tomographic reconstruction in previous studies (Kapadia 2007, Floyd *et al* 2008, Lakshmanan and Kapadia 2012).

**Table 3.** Isotopes of interest in RCC along with their respective energy levels used to generate sinograms from three different regions of interest.

| Region | Isotope | Energy (MeV) | | |
|---|---|---|---|---|
| Background | $^{12}$C | 4.439 | | |
| | $^{14}$N | 2.312 | | |
| | $^{32}$S | 1.548 | 2.230 | 4.281 |
| RCC | $^{31}$P | 1.266 | 2.233 | |
| Healthy kidney | $^{23}$Na | 0.439 | | |
| | $^{39}$K | 2.522 | | |

### 2.4. Data analysis

To demonstrate the ability of NSECT in detecting RCC, the tomographic reconstructions were evaluated both qualitatively and quantitatively as discussed below.

In the qualitative approach, we first visualized the differences in element composition between healthy and RCC kidney compositions using multiple image reconstructions from four different isotopes. The images corresponding to $^{31}$P, $^{39}$K and $^{23}$Na, which occurred predominantly in the kidneys, were superimposed individually with an image from $^{32}$S, which was prevalent in the background. This superimposed image represented the reconstruction for one slice of the scan. Ten such slices were reconstructed and volume rendered into a single 3D image to evaluate the extent of RCC inside the body. The volume-rendered 3D map considered the healthy kidney, the background tissue composition, as well as the tumorous kidney tissue. The volume rendering was performed using MATLAB (2012).

According to the physical principles of NSECT, all tomographic images must be interpreted as a spatial distribution of specific isotopes under evaluation one at a time. However, unless the images represent an isotope whose concentration and location are unique to an organ, the conventional NSECT technique cannot be used to isolate the organ's anatomy within the reconstructed image. Instead, a combination of isotopes that appear in the organ in specific ratios can be used to isolate or differentiate organs within the body even if the isotopes are present in other regions of the image. We demonstrate this principle through the following methodology.

First, to quantify the difference between the concentrations of RCC-associated isotopes in the kidneys, images from each isotope were analyzed within the regions corresponding to the kidney. The kidney regions were isolated using a binary mask that was obtained from images corresponding to $^{12}$C, $^{32}$S and $^{14}$N. These three isotopes were selected because they appeared in most organs in the body in different ratios in each tissue as described in tables 1 and 2. Therefore, the anatomic information of the irradiated tissues can be recovered using a proper mathematical combination of these images based on the known mass fractions of the isotopes.

The known mass fractions are unique to most organs, and this feature can be explored to distinguish specific organs among the irradiated tissues. For example, the mass fraction of $^{12}$C in the healthy kidney, spleen and soft tissue is 13.0%, 11.1% and 25.6%, respectively. Hence, we expect different image intensities in the regions corresponding to the kidneys, spleen and soft tissue, as seen in figure 3(a). Similarly, the inversion of gray scale in the $^{12}$C image provides a complementary image (figure 3(d)) where the distribution of intensity is inverted, i.e. dark regions become bright. The same feature can be seen for other images from the isotopes $^{14}$N and $^{32}$S, figure 3. The gray scale inversion was used because it allowed us to enhance the visualization of the organs of interest, particularly for combinations of elements that showed high/low concentration in an organ of interest compared to surrounding tissue. In certain cases, an organ of interest such as the liver or kidney showed high concentration
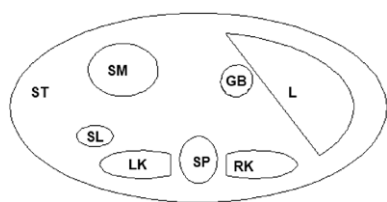
**Figure 2.** Template of the central slice. Labels are provided for tissue identification: L = liver, GB = gallbladder, SP = spine, SL = spleen, SM = stomach, ST = soft tissue, LK = left kidney (RCC) and RK = right kidney (healthy).

(and therefore high pixel value) for certain elements such as C, and N, and low concentration (and low pixel value) for elements such as S. Therefore, when the images for these different elements were combined, the high/low pixel values would negate each other, and the organ of interest could not be visualized over the surrounding background. Inverting the gray scale for these elements enhanced the visualization of the organ region in the combinatorial images.

The linear operation associated with inversion of gray scale was applied to the images from $^{12}$C, $^{32}$S and $^{14}$N in order to enhance the location of the kidneys. After the gray scale inversion, the stack of tomographic images for each isotope was normalized to a 0–1 scale. Then, the three set of tomographic images were multiplied pixel by pixel, giving as a result a stack of images in which the kidneys were highlighted clearly (figure 4(a)). As a final step, the binary images were acquired by establishing a threshold to obtain the best visual representation of regions belonging to the kidneys regarding the modeled kidneys and the reconstructed images, respectively figures 2 and 4(b).

This procedure was applied to all images reconstructed for these three isotopes to distinguish the kidneys from other tissues and organs in the image. Once the kidneys were identified within the torso, a statistical test was evaluated in order to evaluate the difference between the concentrations of isotopes associated to RCC and healthy kidney, i.e. $^{31}$P, $^{39}$K and $^{23}$Na. To ensure that the same number of pixels was sampled in each image, three ROIs composed of $3 \times 3 \times 10$ pixels were applied across all images in the 10 cm stack. The first two were positioned in the center of each kidney to avoid sampling regions of the kidney edge, which could contain artifacts and shadowing effects from photons scattered from the spine and other organs. The third ROI was then positioned outside the kidneys to sample pixel values unrelated to the kidney composition. The locations of ROIs are indicated in figure 4(b) for the central slice. The average gray level in each ROI was compared against each other using the *t*-test for difference of means. Two-tailed *p*-values $\leqslant 0.05$ (95% confidence level) were considered significant. Figure 4(b) shows the position of the ROIs in a single slice of the binary mask for kidneys.

## 3. Results and discussion

### 3.1. Kidney identification in images

The images presented in this section were acquired according to section 2.4 in which we presented the methodology developed to distinguish the kidneys from other tissues and organs in the image. A schematic of the central slice of the human torso, which was illuminated by the neutron beam is shown in figure 2. The main organs are indicated by labels (defined in the figure caption). The tomographic images reconstructed based on the anatomy displayed in the central slice is shown in figure 3.
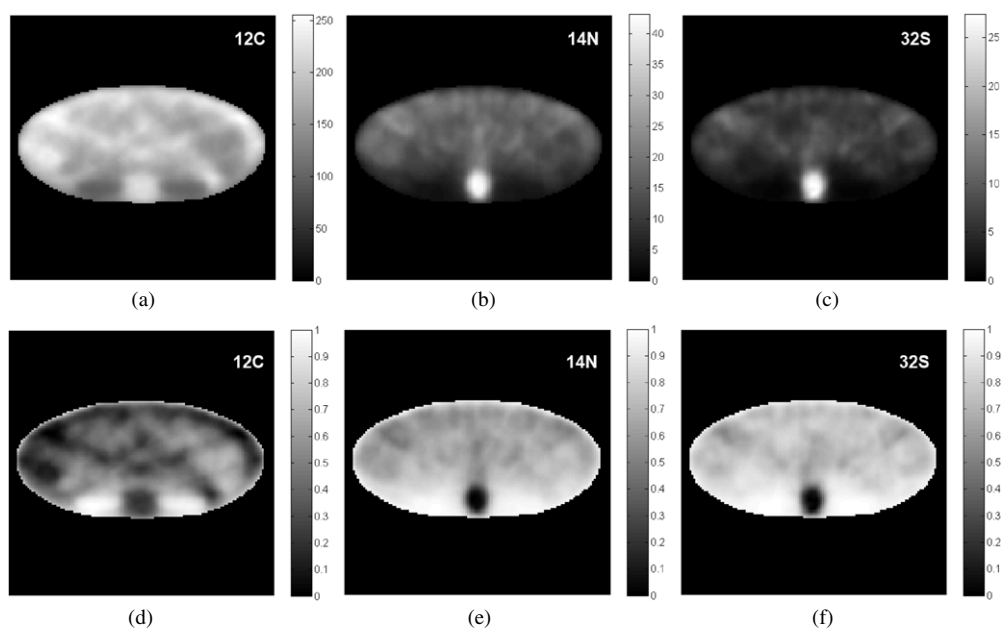
**Figure 3.** Figures (a)–(c) and (d)–(f) show the central slice of the set of tomographic reconstructions respectively from $^{12}$C, $^{14}$N and $^{32}$S. Also shown are the respective inversion of gray scale value from the stack of images that were used to generate the binary mask for kidney identification.
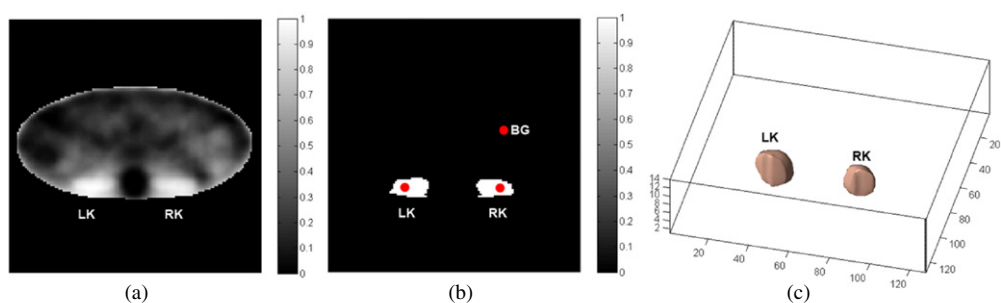


**Figure 4.** Steps of the kidney reconstruction process: (a) normalized image obtained from a weighted combination of $^{12}$C, $^{14}$N and $^{32}$S; (b) binary image obtained by thresholding (a), showing the locations of the kidneys. The red dots represent the ROIs used for the analysis of the mean gray levels in the organ; (c) 3D binary image generated from all slices scanned in the body. This image was used as a mask in subsequent data analysis. RK = right kidney; LK = left kidney; BG = background.

Figure 4(a) shows the image generated as a combination of isotopes multiplying (pixel by pixel) the three stacks of images from $^{12}$C, $^{14}$N and $^{32}$S, as described in section 2.4. From this figure, a binary image was obtained by establishing a threshold that recovered the kidney shape corresponding to the anatomical phantom modeled in our work. The 2D binary image is shown in figure 4(b), and its 3D counterpart, generated by applying the threshold to all images in the stack, is shown in figure 4(c). This 3D mask was used to correlate the spatial distribution of isotopes identified in the NSECT images with the anatomical regions belonging to the kidneys.
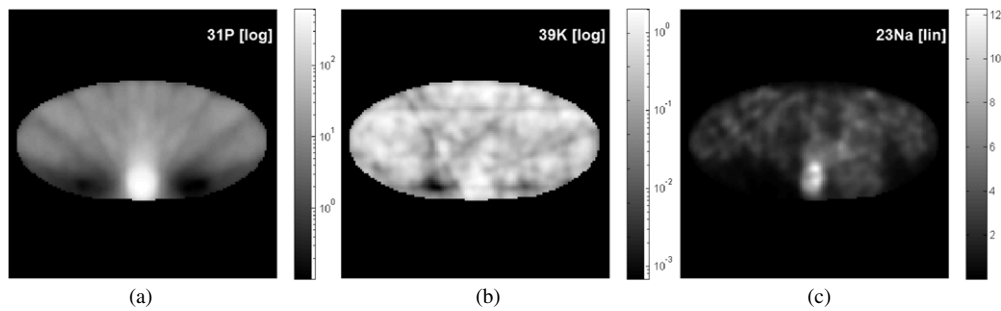
**Figure 5.** Tomographic reconstructions for three isotopes related with RCC and healthy kidney tissue. The images for $^{31}$P and $^{39}$K are shown on a log scale to enhance the image visualization.

### 3.2. Tomographic reconstructions and volume rendering

Figure 5 shows the tomographic images for the three main isotopes associated with RCC and healthy kidney compositions (i.e., $^{31}$P, $^{39}$K and $^{23}$Na) in the central slice.

From figure 5, a clear difference is observed in the gray level of the two kidneys with respect to each other and with the background for all three isotopes. However, the difference in gray level between organs other than kidneys is not visible because the isotopes do not show sufficiently high concentration gradients among these other organs. As a reminder, the gray level in the image directly corresponds to the concentration of the isotope in the organ. Figure 5 thus shows a higher concentration of $^{23}$Na and $^{39}$K in the healthy kidney (right kidney) and a higher concentration of $^{31}$P in the RCC (left kidney); a trend that is in agreement with the material composition for kidneys described in table 1. Therefore, the analysis of such isotopes requires identification of the anatomical location of the kidneys, which was achieved using the binary mask described previously. Also, the mask was created from the same NSECT scan as that used for data analysis, thereby eliminating the need for a second anatomic scan (such as x-ray CT or MRI) for co-registration.

The 3D binary mask was applied on each set of reconstructed images corresponding to $^{31}$P, $^{39}$K and $^{23}$Na. The images from $^{32}$S were used as a background image to provide the phantom's contour. As shown in figure 3(c), the gray level of $^{32}$S is lower in the kidney than in the remainder organs, indicating lower concentration in the kidney. The reconstructed images from $^{31}$P, $^{39}$K and $^{23}$Na were combined with $^{32}$S, one at time, to generate superimposed combinations of $^{32}$S with each of the three other isotopes. This procedure was adopted to re-introduce the background information from the torso (from $^{32}$S), which was otherwise removed by the kidney-specific masks. These superimposed images for the central slice of the irradiated torso are shown in figures 6(a)–(c). The $^{32}$S image is shown in green and the other isotopes are shown in red.

As can be noticed in figures 6(a)–(c), the locations of the highlighted red region for all images are in agreement with the distribution of the isotopes in the kidneys (described in table 1 and shown in figure 5). The figures indicate that the concentrations of $^{23}$Na and $^{39}$K are higher in the healthy kidney (right kidney) than in RCC (left kidney), and the concentration of $^{31}$P is higher in RCC than in the healthy kidney. All of these observations agree with the material composition modeled in the two kidneys. A second qualitative analysis can be provided by averaging the intensities of pixels across all reconstructed slices for each individual isotope. This procedure allows us to suppress the noise and statistical uncertainty from the tomographic reconstructions. The images resulting from averaging are shown in figures 6(d)–(f). As can be observed, the background intensity (based on $^{32}$S) is almost constant across all slices whereas
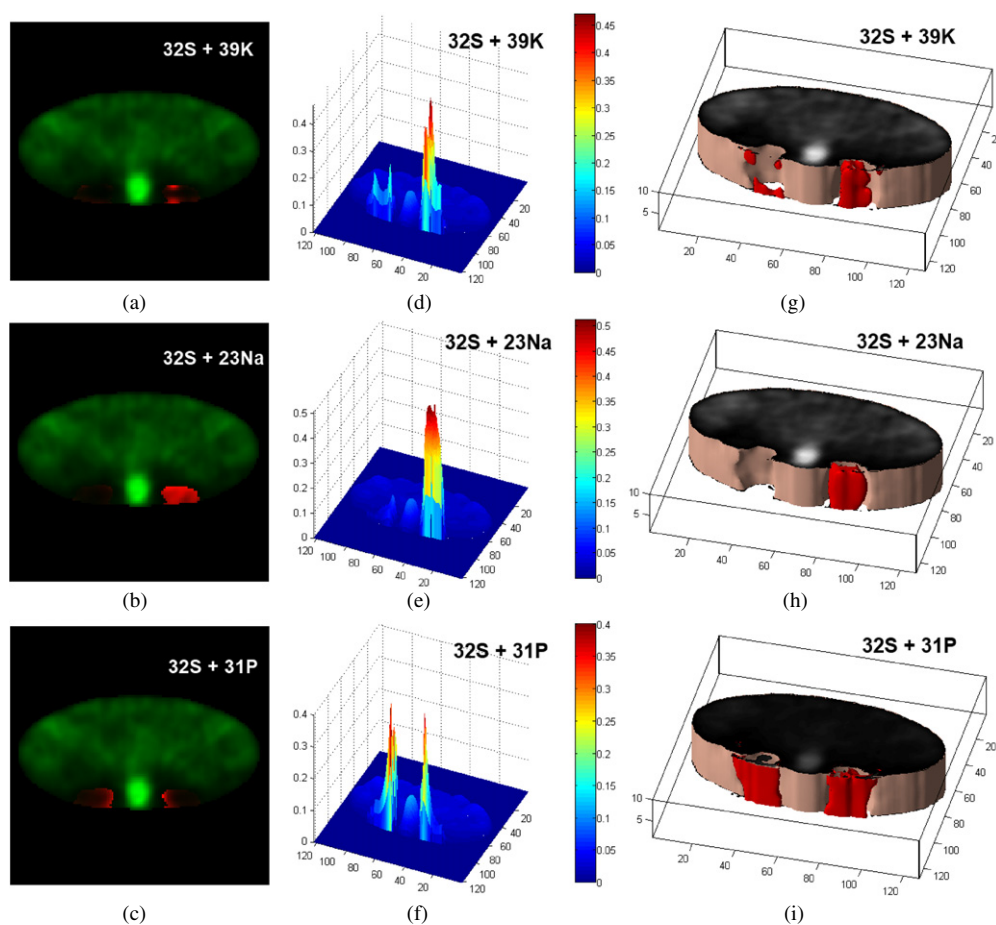
**Figure 6.** Two-dimensional images (left), mean pixel intensities (middle) and volume-rendered 3D images (right) for combinations of four isotopes in the kidneys—$^{32}$S, $^{39}$K, $^{23}$Na and $^{31}$P.

the mean gray level related to the concentrations of $^{39}$K,$^{23}$Na and $^{31}$P within the kidneys changes across slices.

These two sets of images (i.e., figures 6(a)–(c) and (d)–(f)) demonstrate the ability to map the distribution of the isotopes in the organs as well as to quantify the differences in concentration (i.e., the mean gray level) between both kidneys in the entire scan. While 2D images are adequate for quantitative analysis, they cannot be used to evaluate the extent of the lesion in the irradiated volume unless each image is showed side by side. This is an impractical approach in the case of more complex scans. To overcome this limitation, the set of 2D images was used to generate a volume-rendered 3D image using MATLAB. Figures 6(g)–(i) show the volume-rendered images for each pair of isotopes after applying the binary mask (from figure 4(c)).

The 3D images in figures 6(g)–(i) demonstrate the ability to visualize the lesion's extent through a single irradiation of the organ. The external surface of the torso (pink) was rendered using the images from $^{32}$S, which explains the absence of both kidneys (this effect was also visible in figure 3(c)). The inner surface (red) represents the volume corresponding to the combination of isotopes present in the kidneys (material composition in table 1). As in the

**Table 4.** Quantitative analysis for difference of means of pixel value for kidneys and torso.

| Isotope | ROI | Average | Standard deviation | Tested ROIs | $P$-value | Evaluated ratio (LK/RK) | Expected ratio (LK/RK) |
|---------|-----|---------|--------------------|-------------|-----------|-------------------------|------------------------|
| $^{39}$K | LK | 0.01 | 0.01 | LK:BG | <0.05 | | |
| | RK | 0.12 | 0.07 | RK:BG | <0.05 | 0.12 | 0.31 |
| | BG | 0.42 | 0.14 | LK:RK | <0.05 | | |
| $^{31}$P | LK | 0.66 | 0.15 | LK:BG | <0.05 | | |
| | RK | 0.38 | 0.16 | RK:BG | <0.05 | 1.73 | 14.65 |
| | BG | 18.49 | 1.46 | LK:RK | <0.05 | | |
| $^{23}$Na | LK | 0.39 | 0.16 | LK:BG | <0.05 | | |
| | RK | 5.27 | 1.26 | RK:BG | <0.05 | 0.07 | 0.01 |
| | BG | 4.15 | 0.74 | LK:RK | <0.05 | | |

previous images, a difference in intensity is observed between the kidneys for $^{31}$P, $^{39}$K and $^{23}$Na, which agrees with the modeled concentrations of these isotopes in the two kidneys.

### 3.3. Quantification analysis

The images presented in figure 6 allow qualitative analysis of the abundance of the isotopes under evaluation. Based on the material composition shown in table 1, we expect to observe a high-intensity region for $^{23}$Na and $^{39}$K in the right kidney (healthy) and a low-intensity (or no-intensity) region in the left kidney (RCC). In addition to these qualitative analyses, quantitative analysis was performed over the images to evaluate the differences in the composition of the kidneys, both with respect to each other and with respect to the surrounding regions in the torso.

Quantitative analysis (as described in section 2.4) was performed on these images considering ROIs in the two kidneys and in the surrounding torso tissue (as background). The ROIs, shown as red dots in figure 4(b), were selected in regions of the kidneys that were free of shadow effects from the spine. For each evaluated isotope, the average and standard deviations in the ROI were calculated across all reconstructed slices. Then, the mean pixel values for each of the three ROIs were compared to evaluate (a) the ratios between the two kidneys (LK:RK), and (b) the ratios of the kidneys to the torso background (LK:BG and RK:BG).

Table 4 summarizes the findings for the quantitative analysis of the images. As shown in table 4, the mean pixel values of RK and LK were found to be statistically different from each other for all evaluated isotopes. Similarly, the mean pixel value of RK and LK for the evaluated isotopes was also statistically different from BG. The ratio of the pixel intensities in the two kidneys (LK/RK) was found to be in agreement with the increase/decrease trend between the two kidneys, i.e., the images for $^{39}$K and $^{23}$Na showed LK:RK ratios <1, indicating a lower concentration in RCC (LK) than in the healthy kidney (RK), whereas $^{31}$P showed a ratio >1, indicating higher concentration in RCC than in the healthy kidney. However, the actual values of the ratios were different from the expected values computed from the known isotope concentrations (last column of table 4). The discrepancy can be attributed to the concentrations of the isotopes being low, almost at the limit of sensitivity of the NSECT technique. For example, soft tissue has 0.1% of $^{23}$Na whereas RCC lesion has only 0.01%. Although these concentrations are very different from each other, the sensitivity of the current implementation of the NSECT technique is not sufficient to precisely quantify 0.01% level with high accuracy. As a result, the ratio of intensities in the reconstructed images deviates from the expected linear behavior due to errors in quantification of the lower limit. Agasthya
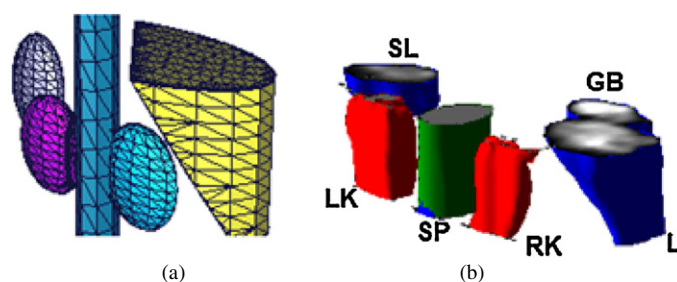
**Figure 7.** 3D template based on the anatomical phantom simulated in our work (a). 3D reconstructions of five different organs in the phantom: left kidney (LK), right kidney (RK), spine (SP), spleen (SL), gallbladder (GB) and liver (L) (b). The liver, spine and gallbladder were not fully reconstructed from the stack of ten scanned slices.

*et al* (2012) have presented an analysis of the sensitivity of the NSECT scan for detection of iron in the liver in which they describe that the sensitivity of detection through NSECT may lie between 0.05% and 0.2% of tissue mass fraction depending on the patient size and number of detectors used. Concentrations above this threshold would follow the linear relationship between signal and concentration.

The sensitivity of the NSECT technique is dependent of the inelastic cross section and the relative abundance of each isotope present in the irradiated media. In addition, the isotopes show different concentration across organs. Therefore, element which have ether low cross section or low concentration could fall below the sensitive of technique. As observed in our results, the low concentration of the isotopes evaluated in this study ($^{39}K$ and $^{31}P$ in both renal tissues and $^{23}Na$ in RCC tissue) fall below this quantification threshold. Hence basing the classification in more than one isotope provides more reliable findings concerning the cancer. This limitation regarding the sensitivity of detection for low concentration elements is being addressed through novel engineering implementations (such as time-resolved imaging and multi-detector encoded acquisition) (Agasthya 2013).

### 3.4. 3D multi-organ reconstruction

Thus far we have shown the ability to correlate the kidney's anatomy with the chemical composition of the tissue determined using the same NSECT scan. This methodology can be extended to other organs as well. That is, if the element composition of an organ is known (even approximately), it is possible to mathematically identify regions showing that particular combination of gray level intensities across the reconstructed images to isolate the anatomy of that organ, lesion or diseased tissue. To demonstrate this concept, the 3D binary mask corresponding to the kidneys (described in section 3.1) was extended to other organs based on the combination of isotopes in those organs, figure 7.

The spine was reconstructed by thresholding the image of $^{32}S$ (figure 3(c)). Due to the high density of spine, the $^{32}S$ signal is strong enough to be reconstructed by itself without any contributions from other isotopes. (Note. The spine reconstruction could also have been performed using the isotope $^{40}Ca$, which is abundant in bone tissue; however, this isotope was not evaluated in the current study).

The spleen, gallbladder and liver were reconstructed using a combination of $^{12}C$ and the image shown in figure 4(a) (combination of isotopes $^{12}C$, $^{14}N$ and $^{32}S$). The stack of images from $^{12}C$ (figure 3(a)) was normalized to a 0–1 scale and then multiplied by its gray scale inversion (figure 3(d)) (I). Then, the stack of images from the combination of isotopes $^{12}C$,

**Table 5.** Dosimetry analysis for the NSECT scan calculated using MCNP5 code. The label '*' denotes organs that are grouped together as 'remainder' tissues in ICRP (2009).

| Tissue | MeV g$^{-1}$ ($\times 10^7$ neutrons) | Absorbed dose (mGy) | Equivalen dose (mSv) | $w_T$ | Effective organ dose (mSv) |
|---|---|---|---|---|---|
| Directly irradiated | | | | | |
| Liver | 0.63 | 1.01 | 13.13 | 0.04 | 0.53 |
| Stomach | 0.57 | 0.92 | 11.94 | 0.12 | 1.43 |
| Spine | 0.15 | 0.24 | 3.13 | 0.12 | 0.38 |
| Kidney* | 1.40 | 2.24 | 29.10 | | |
| Pancreas* | 0.86 | 1.37 | 17.79 | | |
| Spleen* | 0.97 | 1.55 | 20.19 | 0.12 | 1.45 |
| Gallbladder* | 0.66 | 1.06 | 13.75 | | |
| Scattered radiation | | | | | |
| Lung | 0.02 | 0.03 | 0.43 | 0.12 | 0.05 |
| Testis | 0.01 | 0.01 | 0.01 | 0.08 | 0.01 |
| Pelvis | 0.01 | 0.01 | 0.17 | 0.12 | 0.02 |
| Bladder | 0.01 | 0.01 | 0.07 | 0.04 | 0.01 |
| Intestine* | 0.13 | 0.21 | 2.73 | | |
| Thymus* | 0.01 | 0.01 | 0.06 | | |
| Adrenal* | 0.97 | 1.56 | 20.25 | 0.12 | 1.45 |
| Heart* | 0.02 | 0.03 | 0.45 | | |
| Soft tissue* | 0.21 | 0.33 | 4.34 | | |

Total effective dose from ten-slice scan = 3.86 mSv.

$^{14}$N and $^{32}$S (II), (figure 4(a)), was subtracted from the normalized $^{12}$C image, i.e. (I)–(II). The reader may notice that we used twice the images from $^{12}$C; however, the information acquired from (I) and (II) are different, even though they are based on the same isotope. Image (I) is able to enhance the location of organs such as kidneys, spleen, gallbladder and liver, whereas image (II) highlights predominantly the kidneys. Therefore, the linear operation (I)–(II) allows the kidneys to be suppressed and emphasizes the remaining organs other than soft tissue. The same procedure could be carried out using a different combination of isotopes than $^{12}$C, $^{14}$N and $^{32}$S since their concentrations among tissues are high enough to recover the boundaries between organs. Hence, the resultant images represent a mathematical combination of the images corresponding to each individual isotope.

A threshold was also applied on the difference image (i.e., (I)–(II)) to obtain the best visual representation of the reconstructed organs based on the anatomical phantom modeled in our work (figure 7(a)). Figure 7(b) shows the composite image of all organs in the torso reconstructed using this methodology. Each organ was reconstructed individually using a unique combination of its known isotopes, and the reconstructed images were fused to create the organ map shown in figure 7(b). The image demonstrates that through a single 3D tomographic scan based on the NSECT technique, it is possible to associate the disease state of tissues with the anatomical location of the corresponding organ and therefore correlate both anatomical and chemical information.

*3.5. Dosimetry*

The MCNP5 code is capable of evaluating the average energy deposition in target volumes considering all interactions in the tissue from the incident particles. The energy deposition was calculated using the tally F6:N,P in MCNP5, which considers the interactions of neutrons, photons and electrons with the irradiated sample and provides deposited energy in units of MeV g$^{-1}$ per source particle.

The average dose per organ and average total body dose were calculated across all 6 000 beam positions. Seven organs were illuminated directly by the neutron beam during the scanning: liver, kidneys, pancreas, spine, spleen, stomach and gallbladder. In addition nine other organs and tissue groups were out of the neutron beam path and only received scattered radiation: lung, testis, pelvis, bladder, intestine, thymus, adrenal, heart and soft tissue. The average effective dose per organ was evaluated for all of these organs and tissue groups, i.e., the seven organs irradiated directly, the eight organs receiving scattered dose, and the soft-tissue group. The individual organ doses were then summed to determine the average effective dose for the full NSECT scan. Dosimetry was performed in two steps: (a) computing the absorbed dose through MCNP5, and (b) converting the absorbed dose to equivalent organ dose using radiation-weighting and tissue-weighting factors.

The average effective dose per organ (in mSv) was calculated by multiplying the absorbed dose with the radiation-weighting factor (13 for neutrons at 5 MeV) and the tissue-weighting factor $w_T$ for each organ obtained from ICRP (2009). Table 5 presents the absorbed dose and the equivalent organ dose values for the total NSECT scan for all organs in the body. The average effective dose from a ten-slice NSECT scan was found to be less than 4 mSv. For comparison, a typical abdominal CT exam delivers 10 mSv to the average-sized adult (RSNA 2013). The MCNP5 results were normalized to a source intensity of $10^7$ neutrons per projection. All dose values were calculated with a maximum permissible error of 0.2%.

## 4. Conclusion

This study was conducted to demonstrate the ability of the NSECT technique to quantitatively image the differences in element composition between RCC and healthy kidney tissue *in vivo*. The task was achieved using Monte Carlo simulations in MCNP5. Using an MCNP5 simulation of a tomographic system for NSECT, we demonstrated the ability to generate 3D images of healthy and cancerous kidneys based on a combination of elements present in the organs. While the current work used isotopes that occurred in high concentration (i.e., $^{12}$C, $^{32}$S and $^{14}$N), the same task could be achieved for other low-concentration isotopes present in any organ of interest, provided their concentration was above the sensitivity threshold of the imaging system. The imaging and reconstruction results in our study showed that despite the concentrations of the isotopes being too low for accurate quantification, the images showed agreement in the increase/decrease trend related to isotopes studied in the kidney, i.e. $^{31}$P, $^{39}$K and $^{23}$Na. Furthermore, this task was achieved using dose that was less than the dose of a clinical CT scan.

Based on our findings, we concluded that the NSECT technique has the ability to detect the difference of composition between the healthy and diseased kidneys and generate a 3D anatomical map of human body based only on the natural elemental composition of each organ. The next step for this work involves evaluating parameters related to the practical clinical applications of NSECT, for example, the sensitivity and quantification accuracy for the elements under evaluation, the overall system design with respect to the source and detector configuration, and optimizing the acquisition protocol to reduce radiation dose even further.

## Acknowledgment

# References

ACN 2013 What are the key statistics about kidney cancer? (Atlanta, GA: American Cancer Society) available at www.cancer.org/cancer/kidneycancer/detailedguide/kidney-cancer-adult-key-statistics (accessed 06 April 2013)

Agasthya G 2013 Low-dose imaging of liver diseases through neutron stimulated emission computed tomography: simulations in GEANT4 *PhD Thesis* Duke University

Agasthya G A, Harrawood B C, Shah J P and Kapadia A J 2012 Sensitivity analysis for liver iron measurement through neutron stimulated emission computed tomography: a Monte Carlo study in GEANT4 *Phys. Med. Biol* **57** 113–26

Altekin E, Coker C, Sisman A R, Onvural B, Kuralay F and Kirimli O 2005 The relationship between trace elements and cardiac markers in acute coronary syndromes *J. Trace Elem. Med. Biol.* **18** 235–42

Calvo F B, Santos Junior D, Rodrigues C J, Krug F J, Marumo J T, Schor N and Bellini M H 2009 Variation in the distribution of trace elements in renal cell carcinoma *Biol. Trace Elem. Res.* **130** 107–13

Chmielnicka J and Nasiadek M 2003 The trace elements in response to lithium intoxication in renal failure *Ecotoxicol. Environ. Saf.* **55** 178–83

Cohen H T and Mcgovern F J 2005 Renal-cell carcinoma *New Engl. J. Med.* **353** 2477–90

Cristy M and Eckerman F 1987 Specific absorbed fractions of energy at various ages from internal photon sources: I. Methods *Ridge National Laboratory Report* ORNL/TM-8381/VI

Dobrowolski Z, Drewniak T, Kwiatek W and Jakubik P 2002 Trace elements distribution in renal cell carcinoma depending on stage of disease *Eur. Urol.* **42** 475–80

Floyd C E Jr, Bender J E, Sharma A C, Kapadia A, Xia J, Harrawood B, Tourassi G D, Lo J Y, Crowell A and Howell C 2006 Introduction to neutron stimulated emission computed tomography *Phys. Med. Biol.* **51** 3375–90

Floyd C E Jr *et al* 2008 Neutron-stimulated emission computed tomography of a multi-element phantom *Phys. Med. Biol.* **53** 2313–26

Floyd C E Jr *et al* 2007 Neutron stimulated emission computed tomography: background corrections *Nucl. Instrum. Methods Phys. Res.* B **254** 329–36

ICRP 2009 Adult reference computational phantoms *ICRP Report* 103 (Ottawa: ICRP)

ICRU 1992 Photon, electron, proton and neutron interaction data for body tissues *ICRU Report* 46 (Bethesda, MD: ICRU)

Kapadia A 2007 Accuracy and patient dose in neutron stimulated emission computed tomography for diagnosis of liver iron overload: simulations in GEANT4 *PhD Thesis* Duke University

Kapadia A J, Sharma A C, Tourassi G D, Bender J E, Howell C R, Crowell A S, Kiser M R, Harrawood B P, Pedroni R S and Floyd C E Jr 2008a Neutron stimulated emission computed tomography for diagnosis of breast cancer *IEEE Trans. Nucl. Sci.* **55** 501–9

Kapadia A J, Tourassi G D, Sharma A C, Crowell A S, Kiser M R and Howell C R 2008b Experimental detection of iron overload in liver through neutron stimulated emission spectroscopy *Phys. Med. Biol.* **53** 2633–49

Kim E Y, Park B K, Kim C K and Lee H M 2010 Clinico-radio-pathologic features of a solitary solid renal mass at MDCT examination *Acta Radiol.* **51** 1143–8

Kim J I, Cho J Y, Moon K C, Lee H J and Kim S H 2009 Segmental enhancement inversion at biphasic multidetector CT: characteristic finding of small renal oncocytoma *Radiology* **252** 441–8

Kim J K, Park S Y, Shon J H and Cho K S 2004 Angiomyolipoma with minimal fat: differentiation from renal cell carcinoma at biphasic helical CT *Radiology* **230** 677–84

Kim J Y, Kim J K, Kim N and Cho K S 2008 CT histogram analysis: differentiation of angiomyolipoma without visible fat from renal cell carcinoma at CT imaging *Radiology* **246** 472–9

Lakshmanan M N and Kapadia A J 2012 Quantitative assessment of lesion detection accuracy, resolution, and reconstruction algorithms in neutron stimulated emission computed tomography *IEEE Trans. Med. Imaging* **31** 1426–35

Lange K and Carson R 1984 EM reconstruction algorithms for emission and transmission tomography *J. Comput. Assist. Tomogr.* **8** 306–16

MathWorks Inc. 2012 MATLAB Version 8.0 (R2012b) (Natick, MA: MathWorks)

Millet I, Doyon F C, Hoa D, Thuret R, Merigeaud S, Serre I and Taourel P 2011 Characterization of small solid renal lesions: can benign and malignant tumors be differentiated with CT? *Am. J. Roentgenol.* **197** 887–96

Mutter J 2008 Mercury and Alzheimer's disease *Fortschr. Neurol. Psychiatr.* **76** 170–2

Neuzillet Y, Lechevallier E, Andre M, Daniel L and Coulange C 2004 Accuracy and clinical role of fine needle percutaneous biopsy with computerized tomography guidance of small (less than 4.0 cm) renal masses *J. Urol.* **171** 1802–5

NUDAT 2013 NuDat 2.6—nuclear structure and nuclear decay data available at www.nndc.bnl.gov/nudat2/ (accessed 04 July 2013)

Pandharipande P V, Gervais D A, Hartman R I, Harisinghani M G, Feldman A S, Mueller P R and Gazelle G S 2010 Renal mass biopsy to guide treatment decisions for small incidental renal tumors: a cost-effectiveness analysis *Radiology* **256** 836–46

Remzi M and Marberger M 2009 Renal tumor biopsies for evaluation of small renal tumors: why, in whom, and how? *Eur. Urol.* **55** 359–67

Rizk S L and Sky-Peck H H 1984 Comparison between concentrations of trace elements in normal and neoplastic human breast tissue *Cancer Res.* **44** 5390–4

RSNA 2013 Patient safety: radiation dose in x-ray and CT exams available at:www.radiologyinfo.org/en/safety/index.cfm?pg=sfty_xray (accessed 04 July 2013)

Schmidbauer J, Remzi M, Memarsadeghi M, Haitel A, Klingler H C, Katzenbeisser D, Wiener H and Marberger M 2008 Diagnostic accuracy of computed tomography-guided percutaneous biopsy of renal masses *Eur. Urol.* **53** 1003–11

Verma S K, Mitchell D G, Yang R, Roth C G, O'kane P, Verma M and Parker L 2010 Exophytic renal masses: angular interface with renal parenchyma for distinguishing benign from malignant lesions at MR imaging *Radiology* **255** 501–7

Viana R and Yoriyaz H 2011 NSECT applied to the assessment of calcium deposition due to the presence of microcalcifications associated with breast cancer *Rev. Bras. Fis. Med.* **5** 41–6

X-5 Monte Carlo Team 2003 MCNP—a general Monte Carlo *N*-particle transport code version 5: volume I. Overview and theory X-5 Monte Carlo Team. *Los Alamos National Laboratory Report* LA-UR-03-1987

Zhang J, Lefkowitz R A, Ishill N M, Wang L, Moskowitz C S, Russo P, Eisenberg H and Hricak H 2007 Solid renal cortical tumors: differentiation with CT *Radiology* **244** 494–504